

# Beyond LSDA and Thomas-Fermi: A Hartree-Fock Analysis of Spherical Nanoparticles in the Jellium Approximation

Michael Píro\* and Jaroslav Hamrle

*Department of Solid State Engineering, Faculty of Nuclear Sciences and Physical Engineering,  
Czech Technical University, Trojanova 13, Prague, Czech Republic*

(Dated: July 8, 2025)

A comprehensive Hartree-Fock analysis of the ground-state electronic structure of spherical gold nanoparticles modeled within the jellium approximation is carried out for all systems containing up to 132 delocalized electrons. Emphasis is placed on resolving the energy-level ordering, properly describing the electron density tail and associated charge spill-out, and assessing the accuracy of local exchange and kinetic energy potentials. The calculations are performed on a high-resolution real-space grid to ensure numerical precision. Significant discrepancies are observed between the exchange energy given by the Hartree-Fock approximation and the local spin density approximation (LSDA) in both the inner and outer regions of the nanoparticle. To address these differences, a refined expression of the one-electron exchange energy density as an explicit function of the charge density is proposed. Similarly, the failure of the Thomas-Fermi kinetic energy model near the surface of the nanoparticle is resolved by introducing an improved expression for the one-electron kinetic energy density.

## I. INTRODUCTION

Nanoparticles of different sizes and shapes are known to exhibit fundamentally different optical, magnetic, and catalytic properties compared to their bulk material counterparts [1–4]. These properties arise from the confinement of electrons at the nanoscale and are essential for a wide range of modern technological applications, including drug design and delivery, and bioimaging in medicine [5, 6], photocatalysis [7], or surface-plasmon-based sensing [8]. The rapid development of nanofabrication techniques has increased the demand for theoretical models that can accurately predict the behavior of electronic states in nanoparticles with high precision and minimal computational cost.

A complete quantum-mechanical description of multi-electron nanoparticles quickly becomes intractable as system size increases. To address this, simplified models have been developed that still capture the essential physics. One widely used approach is the spherical jellium model, where the discrete ion background is approximated as a uniform positive charge distribution [9, 10]. This model has been particularly successful in describing the delocalized conduction electrons of alkali-metal clusters. The work focused mainly on the use of density functional theory (DFT) methods to calculate energy spectra [11–14], although several special cases of closed shells in sodium clusters were calculated using the Hartree-Fock approximation [15–17].

Beyond standard DFT, alternative approaches such as quantum hydrodynamic models (QHD) [18, 19] and quantum-corrected classical models (QCM) [20, 21] have gained traction, particularly in the field of plasmonics. These methods treat the electron fluid collectively, while

incorporating quantum effects such as the Bohm potential or pressure terms derived from the kinetic energy density. They enable simulations of larger systems and dynamical phenomena, but their precision is heavily based on the quality of the input energy functionals.

A common limitation of both the DFT and QHD models lies in the exchange and kinetic energy functionals used. In particular, the local spin density approximation (LSDA) can lose its accuracy significantly on surfaces of spatially confined systems [22]. More advanced generalized gradient approximations (GGAs) such as the Perdew-Burke-Ernzerhof functional (PBE) offer limited improvements when the electron density gradient is small relative to the density itself. Similarly, the Thomas-Fermi kinetic energy functional severely underestimates surface effects, failing to describe the electron spill-out or electron density decay rate outside the nanoparticle.

In this work, we address these limitations by explicitly computing the ground-state electronic structure of spherical gold nanoparticles in the finite jellium model using the Hartree-Fock approximation for systems with up to 132 delocalized electrons. Electrons are added one by one to correctly determine the energy-level ordering. Upon analyzing the energy spectra and the shapes of the electron densities, we calculate the one-electron exchange and kinetic energy densities and find appropriate fits to express them as functions of the electron density.

For simplicity, we adopt Hartree atomic units throughout the text.

## II. MODEL DESCRIPTION

In the finite spherical jellium model, the nanoparticle is treated as a solid ball of radius  $R$  composed of  $N$  atoms. Each atom contributes a positively charged ionic core (consisting of the nucleus and tightly bound inner electrons) and  $\nu$  delocalized electrons. The positive charge

---

\* michael.piro@fjfi.cvut.cz

is assumed to be uniformly distributed throughout the interior of the ball, resulting in the ionic charge density:

$$n_{\text{I}}(\mathbf{r}) = \begin{cases} n_{\text{I}} & |\mathbf{r}| \leq R \\ 0 & |\mathbf{r}| > R, \end{cases} \quad (1)$$

where  $n_{\text{I}}$  is the background density constant. The total positive charge, given by  $Q = \nu N$ , can then be expressed as  $Q = \frac{4}{3}\pi R^3 n_{\text{I}}$ . Taking into account the original crystalline arrangement of the atoms, the radius  $R$  is related to the number of atoms by  $R = r_s N^{1/3}$ , where  $r_s$  is the Wigner-Seitz radius. Substituting this into the expression for  $Q$ , the ionic density constant becomes:

$$n_{\text{I}} = \frac{3}{4\pi} \frac{\nu}{r_s^3}. \quad (2)$$

As shown in the Supplementary Material, Section S1, this positive background creates the electrostatic *nanoparticle potential*  $V(r)$ :

$$V(r) = \begin{cases} \frac{\nu}{r_s^3} \frac{r^2 - 3R^2}{2} & r \leq R \\ -\frac{\nu}{r_s^3} \frac{R^3}{r} & r > R. \end{cases} \quad (3)$$

Its shape is depicted in Fig. 1. The parameters  $r_s$  and  $\nu$  depend on the specific material. In this study, we focus on gold atoms, where only the 6s electron is treated as delocalized. This yields  $r_s = 3.01$  Bohr and  $\nu = 1$ .

The system of a single electron in the nanoparticle potential is spherically symmetric. The electron wave function is therefore separated into its angular and radial components:

$$\psi_{nlm}(r, \theta, \phi) = \frac{1}{r} u_{nl}(r) Y_l^m(\theta, \phi), \quad (4)$$

where  $n$ ,  $l$ , and  $m$  denote the principal, azimuthal, and magnetic quantum numbers, respectively. Since the angular wave functions  $Y_l^m(\theta, \phi)$  are determined analytically and are independent of the shape of the radial potential  $V(r)$ , we further examine only the radial components.

To address the multi-electron problem, we add the electron-electron interaction to the Hamiltonian. This is given by the potential  $V_{\text{e-e}}$ , which accounts for all pairwise interactions between electrons:

$$V_{\text{e-e}}(\mathbf{r}_1, \dots, \mathbf{r}_N) = \sum_{\substack{i,j=1 \\ i < j}}^N V_2(\mathbf{r}_i, \mathbf{r}_j) = \sum_{\substack{i,j=1 \\ i < j}}^N \frac{1}{|\mathbf{r}_i - \mathbf{r}_j|}. \quad (5)$$

Next, the spatial one-electron wave function is extended to include spin. We consider the electrons to be only fully in the spin-up or spin-down state. The total many-electron wave function is given by the Slater determinant. The interaction potential then decomposes into two distinct contributions: the Hartree potential  $\hat{V}_{\text{H}}$  and the

exchange potential  $\hat{V}_{\text{x}}$ , defined as:

$$\hat{V}_{\text{H}}\psi_i(\mathbf{r}) = \sum_{\substack{j=1 \\ j \neq i}}^N \int_{\mathbb{R}^3} \psi_j^*(\mathbf{r}') V_2(\mathbf{r}, \mathbf{r}') \psi_j(\mathbf{r}') d\mathbf{r}' \psi_i(\mathbf{r}), \quad (6)$$

$$\hat{V}_{\text{x}}\psi_i(\mathbf{r}) = - \sum_{\substack{j=1 \\ j \neq i}}^N \delta_{s_i s_j} \int_{\mathbb{R}^3} \psi_j^*(\mathbf{r}') V_2(\mathbf{r}, \mathbf{r}') \psi_i(\mathbf{r}') d\mathbf{r}' \psi_j(\mathbf{r}), \quad (7)$$

where  $s_i$  denotes the spin of the  $i$ -th electron. It is important to note that the inclusion of self-interaction terms (contributions with  $i = j$ ) in both  $\hat{V}_{\text{H}}$  and  $\hat{V}_{\text{x}}$  results in their mutual cancellation, leaving the total electron-electron interaction potential unchanged. This small change is useful for the simplification of further calculations.

The one-electron wave functions are again decomposed into their radial and angular parts, as in Eq. (4), now with the addition of the spin quantum number  $s$  to the radial functions. To preserve spherical symmetry of the solution, electrons in partially filled shells are averaged over all quantum numbers  $m$ . In this setting, the Hartree and exchange potentials can be expressed as operators acting solely on the radial wave functions  $u_{nl}^s$  (see Supplementary Material, Section S2):

$$\begin{aligned} \hat{V}_{\text{H}}u_{nl}^s(r) &= \\ &= \sum_{(n', l', s')} N_{n'l'}^{s'} \int_0^{+\infty} u_{n'l'}^{s'}(r')^2 \frac{1}{\max(r, r')} dr' u_{nl}^s(r) \end{aligned} \quad (8)$$

and:

$$\begin{aligned} \hat{V}_{\text{x}}u_{nl}^s(r) &= - \sum_{(n', l')} N_{n'l'}^{s'} \sum_{L=|l-l'|}^{l+l'} \begin{pmatrix} l' & L & l \\ 0 & 0 & 0 \end{pmatrix}^2 \\ &\cdot \int_0^{+\infty} u_{n'l'}^s(r') u_{nl}^s(r') \frac{\min(r, r')^L}{\max(r, r')^{L+1}} dr' u_{n'l'}^s(r), \end{aligned} \quad (9)$$

where  $N_{nl}^s$  is the number of electrons in the shell  $(n, l)$  with spin  $s$ .

### III. ONE-ELECTRON PROBLEM

In order to gain basic insight into the energy spectrum and properties of the wave functions, we will first focus on solving the problem of a single electron in the nanoparticle potential  $V$ . This system can be viewed as the hydrogen atom with a nucleus radius  $R > 0$  and a positive nuclear charge  $Q$ . As a representative example, we consider a nanoparticle of radius  $R = 9.46$  Bohr corresponding to a 1nm nanoparticle. Energies are computed for different values of the azimuthal quantum number  $l$ . The principal quantum number  $n$  is then assigned according to the hydrogenic convention, where for each  $n$ , the allowed values of  $l$  range from 0 to  $n - 1$ . Table I lists

TABLE I. One-electron energy levels of the 1nm nanoparticle for quantum numbers up to  $n = 6$  and  $l = 5$ .

$l$	$n = 1$	$n = 2$	$n = 3$	$n = 4$	$n = 5$	$n = 6$
0	-4.631	-4.248	-3.865	-3.482	-3.104	-2.744
1		-4.439	-4.056	-3.673	-3.292	-2.920
2			-4.248	-3.865	-3.482	-3.103
3				-4.056	-3.673	-3.291
4					-3.865	-3.482
5						-3.673

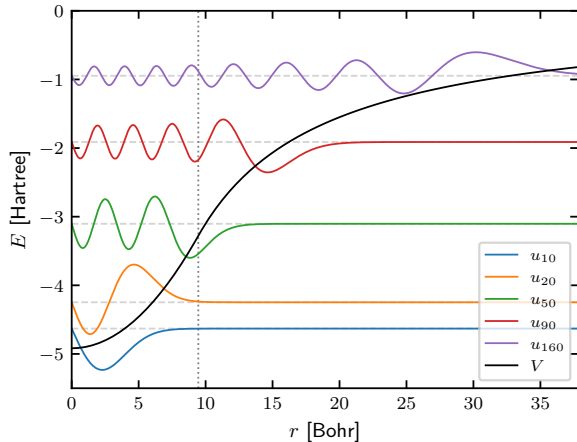


FIG. 1. Nanoparticle potential (black line) and one-electron radial wave functions  $u_{nl}$  for  $n \in \{1, 2, 5, 9, 16\}$  and  $l = 0$  for the 1nm nanoparticle. Horizontal dashed lines indicate corresponding energy levels. Vertical dotted line marks the nanoparticle radius  $R$ .

the computed one-electron energy levels with quantum numbers up to  $n = 6$  and  $l = 5$ . The shapes of several radial wave functions  $u_{nl}$  with angular momentum  $l = 0$  are shown in Fig. 1.

At low energies, the electrons are predominantly localized within the nanoparticle. However, at higher excited states the wave functions extend significantly beyond the particle boundary. The radial wave function has a sinusoidal-like shape, with an increase in both the amplitude and the wavelength outside the particle, decaying to zero from the point where the potential exceeds the corresponding electron energy. Like in the hydrogen atom, the number of radial nodes of the functions  $u_{nl}$  is equal to  $n - l$ .

The effect of the finite nucleus size  $R$  on the energy spectrum is depicted in Fig. 2. We analyze two different settings: First, the total charge  $Q$  is fixed at  $Q = 1$ . Second, the charge density  $n_I$  is fixed by the material constants  $\nu$  and  $r_s$  at  $\nu = 1$ ,  $r_s = 3.01$ . In the first case, we start at  $R = 0$  where the spectrum corresponds to that of the hydrogen atom. As the radius increases, the degeneracy in  $l$  is lifted, breaking the spherical symmetry. In contrast, certain levels, such as  $E_{20}$  and  $E_{32}$ ,

or  $E_{30}$  and  $E_{42}$ , tend to converge. This is evidence of a different degeneracy pattern, namely the one of the harmonic oscillator. This effect is even more profound in the second studied case with a constant positive charge density. Here, the lower-laying electrons converge to an equidistant energy spectrum for increasing radius  $R$ .

Based on these findings and on the shapes of the wave functions, we distinguish two electron energy classes: The energy levels corresponding to the electrons located mainly within the radius of the nanoparticle  $R$ , which we call *harmonic-like*, and energies for which electrons have a significant part of the wave function outside the ionic core. These are called *hydrogen-like*.

## IV. MULTI-ELECTRON PROBLEM

### A. Hund's Rules for Nanoparticles

The first aspect of the multi-electron problem that we examine is the energy level ordering. By incrementally solving the Hartree–Fock equations for increasing electron number  $N$ , we obtained a sequence of occupied orbitals up to  $N = 132$ :

$$1s\ 2p\ 2s\ 3d\ 4f\ 3p\ 5g\ 3s\ 4d\ 6h\ 5f\ 7i. \quad (10)$$

This sequence reveals a notable pattern: for a given principal quantum number  $n$ , orbitals are occupied in order of descending azimuthal quantum number  $l$ . This behavior indicates that the system energetically favors orbitals whose radial wave functions have the fewest possible nodes. As for the spin configurations, a simple rule applies: all available spin-up states are filled before any spin-down states are occupied. This strict alignment of spins results in a net magnetic moment, providing clear evidence that nanoparticles can possess intrinsic magnetic properties. Together, these observations define a set of *Hund's rules for nanoparticles*:

1. for each principal number  $n$ , orbitals are filled in descending order in the azimuthal quantum number  $l$ ,
2. in the partially filled orbitals, spin polarization is maximized.

The evolution of the one-electron Hartree energies  $\epsilon_{nl}$  with  $N$ , shown in Fig. 3, further illustrates the structure of the energy level sequence. As  $N$  increases, the orbital energies generally decrease due to stronger confinement, although small local increases appear for spin-down electrons during the initial filling of each orbital. A particularly notable feature is the reordering of the  $s$  and  $d$  orbitals. We see that the  $3d$  orbital rapidly drops below the  $2s$  level, despite the latter being filled earlier. This inversion can also be observed between levels  $3s$  and  $4d$  and is analogous to the well-known behavior in atomic systems, where  $3d$  orbitals become energetically favorable relative to  $4s$ .

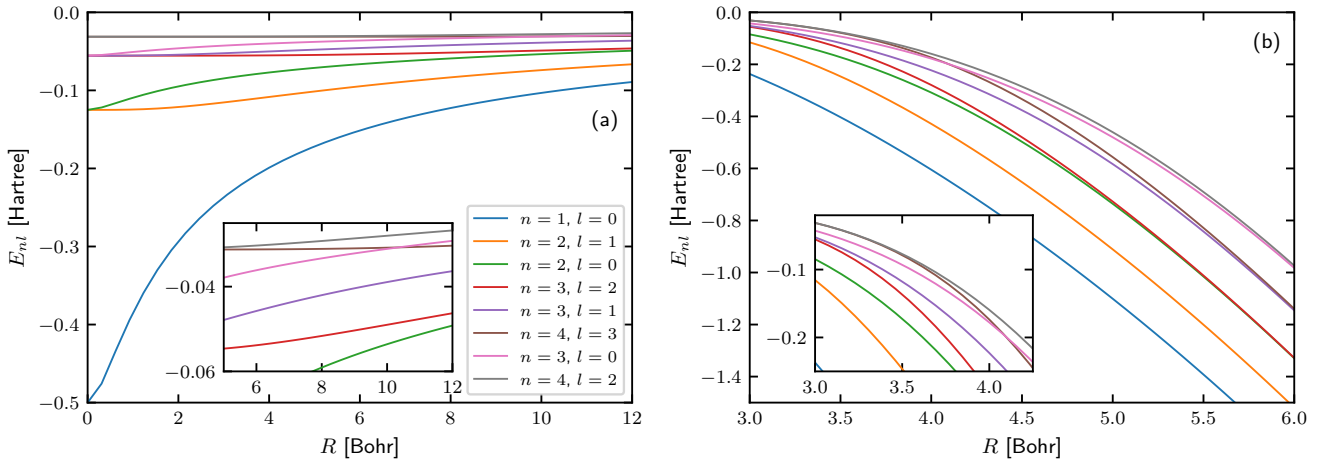


FIG. 2. Dependence of the one-electron energy levels on the radius of the nanoparticle. (a) Total positive charge  $Q$  is fixed at  $Q = 1$ . (b) Positive background charge density  $n_I$  given by Eq. (2) is fixed by the material constants  $\nu$  and  $r_s$  at  $\nu = 1$ ,  $r_s = 3.01$ .

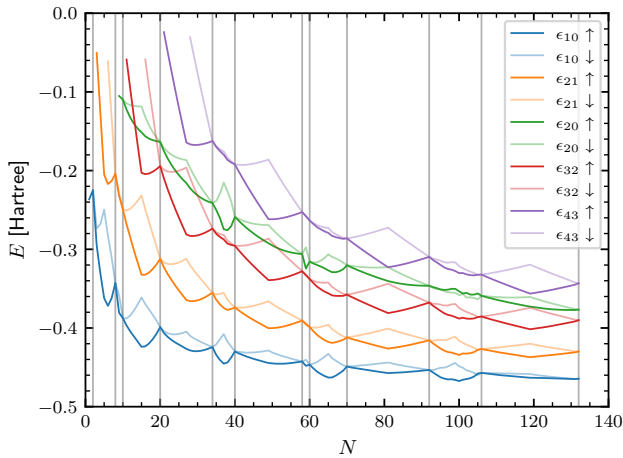


FIG. 3. Evolution of the one-electron Hartree energies  $\epsilon_{nl}$  as a function of electron number  $N$  for the five lowest-energy orbital configurations. Darker and lighter shading indicates spin-up and spin-down electron states, respectively. Grey vertical lines represent the cases with fully filled orbitals.

## B. Energy Contributions

Another important feature of the system we analyze is the total energy and its individual components. Based on their scaling behavior and relative magnitude, the energy contributions can be grouped into two categories: dominant and subdominant terms. The dominant components are shown in Fig. 4. These components include the energy of the interaction between the electrons and the positively charged ionic background  $E_{e-I}$ , the Hartree part of the electron–electron interaction  $E_H$ , and the energy of the ionic background  $E_I$  itself. The ionic back-

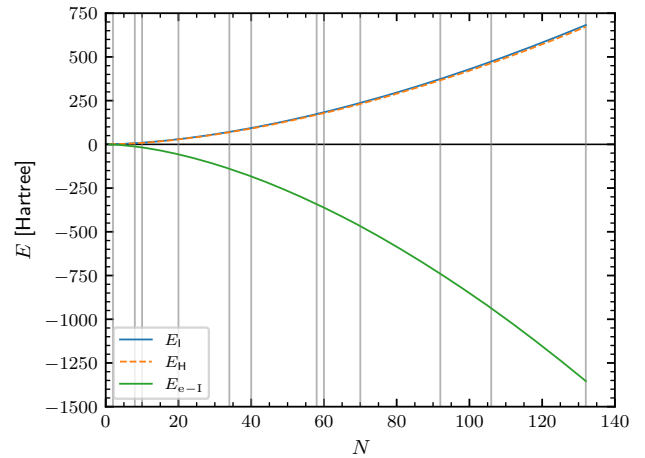


FIG. 4. Dominant energy contributions (ionic background field energy  $E_I$ , electron–ion attraction energy  $E_{e-I}$ , and electron–electron Hartree repulsion energy  $E_H$ ) as functions of the electron number  $N$ . Grey vertical lines represent the cases with fully filled orbitals.

ground energy can be determined analytically and takes the form (see Supplementary Material, Section S1):

$$E_I = \frac{3\nu^2}{5r_s} N^{5/3} = 0.199N^{5/3}. \quad (11)$$

Both  $E_{e-I}$  and  $E_H$  follow a power-law dependence on  $N$  that closely approximates an  $N^{5/3}$  scaling:

$$E_{e-I} \approx -0.380 N^{1.675}, \quad (12)$$

$$E_H \approx 0.182 N^{1.682}. \quad (13)$$

The subdominant contributions, depicted in Fig. 5, include the total kinetic energy  $E_{\text{kin}}$  divided further into

its radial and angular parts  $E_{\text{kin}}^{(\text{rad})}$ ,  $E_{\text{kin}}^{(\text{ang})}$ , and the exchange component of the electron-electron interaction energy  $E_x$ . Both the radial and the angular kinetic en-

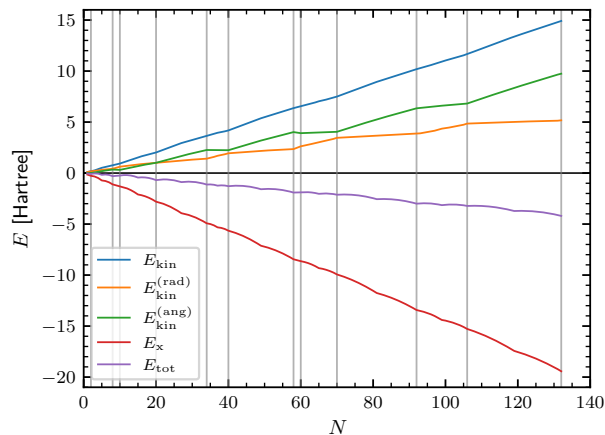


FIG. 5. Subdominant energy contributions (total kinetic energy  $E_{\text{kin}}$ , radial kinetic energy  $E_{\text{kin}}^{(\text{rad})}$ , angular kinetic energy  $E_{\text{kin}}^{(\text{ang})}$ , and electron-electron exchange energy  $E_x$ ) together with the total electrostatic energy  $E_{\text{tot}}$  as functions of the electron number  $N$ .

ergies exhibit sensitivity to the particular energy shell being filled. However, within each orbital, their scaling remains close to linear. Moreover, deviations from a uniform trend in the two components tend to offset each other. Fitting a power-law model to the total kinetic energy and exchange energy thus yields a close linear approximation in  $N$ :

$$E_{\text{kin}} \approx 0.091 N^{1.044}, \quad (14)$$

$$E_x \approx -0.128 N^{1.027}. \quad (15)$$

Finally, the total electrostatic energy of the system also exhibits a close linear approximation in  $N$ :

$$E_{\text{tot}} \approx -0.029 N^{1.011}. \quad (16)$$

Importantly, the dominant terms cancel out almost exactly, with the significance of their sum decreasing with the size of the system. In particular, for the case of  $N = 132$ , the overall contribution of the dominant terms to the total energy is more than 14 times lower than that of the subdominant terms.

### C. Electron Density

Finally, we study the spatial distribution of the electron density. Due to the spherical symmetry of the model, the total electron density depends only on the radial coordinate and is given by:

$$n(r) = \sum_{(n,l,s)} N_{nl}^s \frac{u_{nl}^s(r)^2}{4\pi r^2}. \quad (17)$$

Fig. 6 shows the normalized electron density profiles, defined as  $\bar{n}(r) = n(r)/n_I$ , as functions of the normalized radius  $\bar{r} = r/R$ . The results are presented for nanoparticles with  $N = 58, 92$ , and  $132$ , corresponding to the 7<sup>th</sup>, 10<sup>th</sup>, and 12<sup>th</sup> fully filled shells. All normalized den-

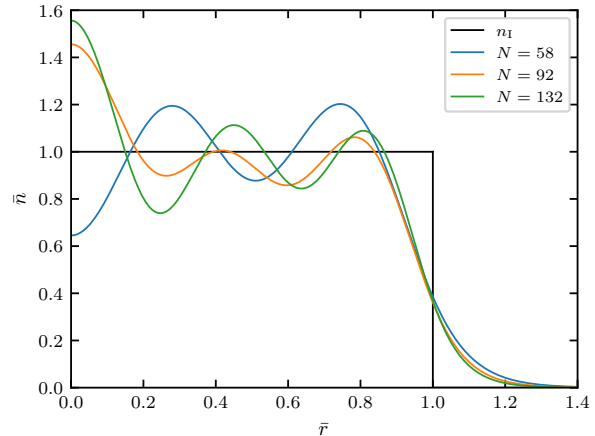


FIG. 6. Radial electron density distributions  $n(r)$ , normalized by the ionic core charge density constant  $n_I$ , as a function of the normalized radius  $\bar{r} = r/R$ , for nanoparticles with  $N = 58, 92$ , and  $132$ .

sity profiles exhibit pronounced oscillations, sometimes called the *Friedel oscillations*, inside the nanoparticle. These are followed by a steep decline near the ionic core boundary and a smooth decay on the outside.

The number of local maxima ranges from one to three, with the most frequent value three appearing in all solutions for  $N \geq 64$ . This observation is a consequence of the fact that electronic functions with the least number of nodes are preferred. The global maximum of the negative charge density is most often located at the first peak and its values reach up to  $1.6 n_I$ . On the other hand, the minimal density on the interior of the nanoparticle is always found at the boundary  $r = R$ , ranging from  $0.25 n_I$  to  $0.41 n_I$ . The relative position of the last peak of the electron density  $\bar{r}_{\text{lm}}$  depending on the number of electrons  $N$  can be estimated as:

$$\bar{r}_{\text{lm}} \approx -c_1 \exp(-c_2 N^{1/3}) + 1, \quad (18)$$

where the fitted coefficients  $c_1$  and  $c_2$  take on the values:

$$c_1 = 0.753, \quad c_2 = 0.280. \quad (19)$$

Although the normalized electron density changes significantly across the observed area, the relative gradient of the electron density in absolute terms  $|\nabla n|/n$  reaches only values of the order  $10^{-2}$ . The density can thus be treated as near-constant on the inside of the nanoparticle.

To accurately handle surface effects and multi-nanoparticle interactions, it is important to properly describe the outside part of the electron density. The normalized density can be well approximated by a decaying

exponential:

$$\bar{n}(r) \approx A_N \exp(-B_N(\bar{r} - 1)), \quad r > R, \quad (20)$$

where  $A_N$ ,  $B_N$  are parameters that depend on the number of electrons  $N$ . Based on these fitted constants, we estimate their shape to be of the form:

$$A_N = -a_1 \exp(-a_2 N^{1/3}) + 0.5, \quad (21)$$

$$B_N = b N^{1/3}, \quad (22)$$

where the fitted coefficients take on the following values:

$$a_1 = 0.254, \quad a_2 = 0.182, \quad b = 2.70. \quad (23)$$

The fraction of electronic charge that resides outside the nanoparticle, the so-called *electronic spill-out*, is defined as:

$$\text{SO} = \frac{4\pi}{Q} \int_R^{+\infty} n(r)r^2 dr, \quad (24)$$

where  $Q = \nu N$  is the total positive charge. Substituting from Eq. (20) for the charge density  $n$ , we obtain an approximate expression for the spill-out in terms of the constants  $A_N$  and  $B_N$ :

$$\text{SO} \approx -3A_N \frac{B_N^2 - 2B_N + 2}{B_N^3} \quad (25)$$

Fig. 7 shows the dependence of the spill-out as a function of  $N$  together with the fitted function, provided by substituting Eqs. (21), (22) for  $A_N$  and  $B_N$  in Eq. (25).

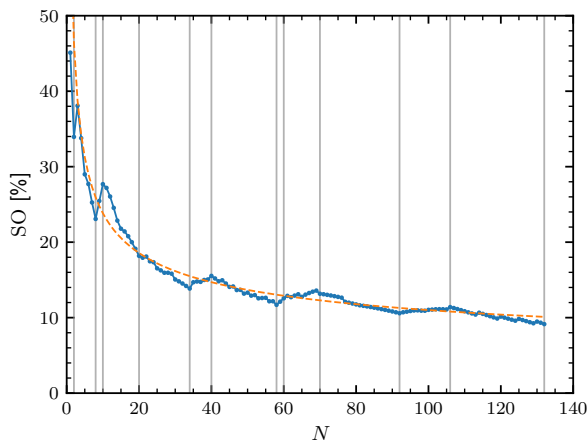


FIG. 7. Fraction of the total electronic charge located outside the nanoparticle radius  $R$  as a function of the electron number  $N$  together with the fitted function given by Eq. (25). Grey vertical lines represent the cases with fully filled orbitals.

## V. EXCHANGE AND KINETIC ENERGIES AS FUNCTIONALS OF THE ELECTRON DENSITY

As established in the section on the energy contributions of the confined multi-electron system, the total energy is determined primarily by the exchange and kinetic components. However, their full quantum-mechanical forms are non-diagonal in orbital or finite real-space grid representations, making direct computation expensive for large systems. In order to use simpler but faster methods for electronic structure calculations, such as DFT or QHD, these operators need to be approximated as functions of the electron density  $n$ .

### A. Exchange energy density

The spin-dependent one-electron exchange energy density  $\varepsilon_x^s(r)$  is defined via the total exchange energy:

$$E_x = 4\pi \sum_s \int_0^{+\infty} \varepsilon_x^s(r) n^s(r) r^2 dr, \quad (26)$$

where  $n^s(r)$  is the electron density corresponding to the electrons with spin  $s$ . We compare this with the exchange energy calculated from the Hartree-Fock equations using the defining relation of the exchange potential Eq. (9). As shown in Supplementary Material, Section S3, this yields an expression for  $\varepsilon_x^s$  in terms of radial wave functions  $u_{nl}^s$ :

$$\begin{aligned} \varepsilon_x^s(r) = & -\frac{1}{2} \left[ \sum_{(n,l)} N_{nl}^s \sum_{(n',l')} N_{n'l'}^s \sum_{L=|l-l'|}^{l+l'} \begin{pmatrix} l' & L & l \\ 0 & 0 & 0 \end{pmatrix}^2 \right. \\ & \cdot \int_0^{+\infty} u_{nl}^s(r') u_{n'l'}^s(r') \frac{\min(r,r')^L}{\max(r,r')^{L+1}} dr' \\ & \left. \cdot u_{nl}^s(r) u_{n'l'}^s(r) \right] / \sum_{(n,l)} N_{nl}^s u_{nl}^s(r)^2. \end{aligned} \quad (27)$$

To find an approximate form of the exchange energy density as an explicit function of the electron density, we construct a parametric plot of  $\varepsilon_x^s(r)$  versus  $n(r)$  (Fig. 8). Within the nanoparticle, both  $n^s$  and  $\varepsilon_x^s$  exhibit non-monotonic behavior, resulting in a cyclic trajectory in the parametric plot. However, these spirals are sufficiently flat to be well approximated by a monotonic functional dependence. To account for possible differences between the inner and outer regions, we fit the energy density function separately. For the interior of the nanoparticle, we use a class of power-law functions of the form:

$$f(x; A, \alpha) = -A x^\alpha. \quad (28)$$

This provides a good model for most of the inner section, but it loses accuracy near the boundary  $r = R$ . In the outer region, no valid fit that provides a meaningful approximation using this function can be found. To address this, we introduce a second family of exponential-type

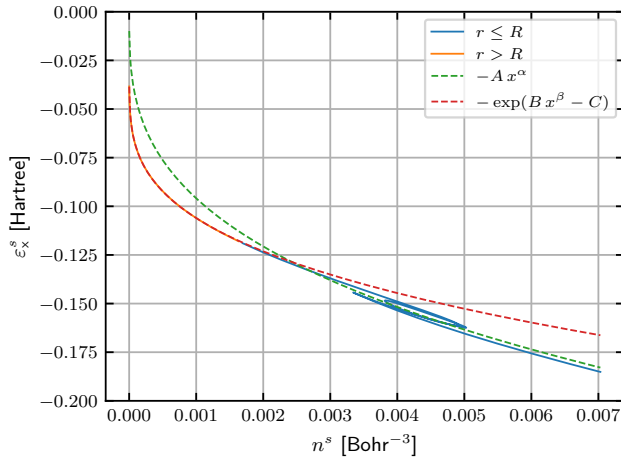


FIG. 8. Dependence of the one-electron exchange energy density  $\varepsilon_x^s(r)$  on the electron density  $n^s(r)$ . The blue color indicates the inner region of the nanoparticle ( $r \leq R$ ), and orange the outer region ( $r > R$ ). Green and red dashed curves represent the fitted functions  $f$  and  $g$ , with parameters  $A = 0.944$ ,  $\alpha = 0.331$ ,  $B = 4.08$ ,  $C = 4.21$ , and  $\beta = 0.1057$ .

functions of the form:

$$g(x; B, C, \beta) = -\exp(Bx^\beta - C). \quad (29)$$

This yields an excellent fit in the outer and near-boundary inner regions, precisely where the power-law approximation fails.

In order to obtain a general formula, we fit both functional classes to the exchange potentials calculated for nanoparticles with electron numbers ranging from  $N = 70$  to  $N = 132$ . The values of the fitted parameters are shown in Fig. S1. Both spin orientations show oscillations around a common mean value, especially in areas of partially filled orbitals. Importantly, deviations of the parameters  $B$  and  $C$  tend to cancel out, providing better stability of the fit. We can therefore define the model of the one-electron exchange energy density for both spin orientations as:

$$\varepsilon_x^s(r) = \min(-An^s(r)^\alpha, -\exp(Bn^s(r)^\beta - C)), \quad (30)$$

where the coefficients are taken as averages over the spin and  $N = 70-132$ . Cases with  $N = 93-97$  and  $N = 100-103$  were excluded due to poor fitting convergence. The specific values of the means and their standard deviations are as follows:

$$A = 0.968 \pm 0.070, \quad (31)$$

$$\alpha = 0.336 \pm 0.014, \quad (32)$$

$$B = 4.31 \pm 0.20, \quad (33)$$

$$C = 4.49 \pm 0.25, \quad (34)$$

$$\beta = 0.0960 \pm 0.0084. \quad (35)$$

Fig. 9 shows the absolute percentage error of the total exchange energy calculated from the electron density

model compared to the results of the Hartree-Fock computation. The model mostly slightly underestimates the

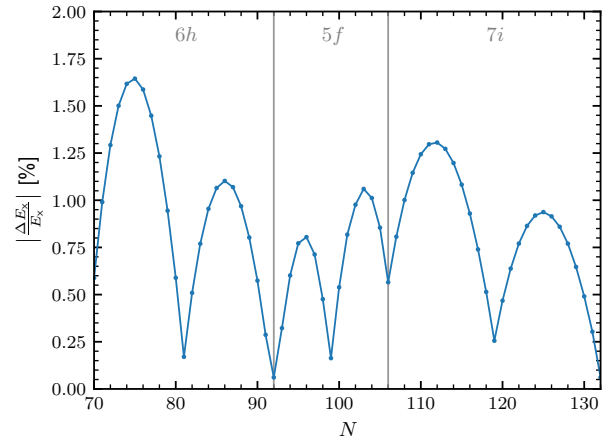


FIG. 9. Absolute percentage error of the total exchange energy of the model given by Eq. (30) compared to the results of the Hartree-Fock computation. Grey vertical lines represent the cases with fully filled orbitals.

energy, with a mean absolute percentage error of 0.84 %. Local minima of the error function are placed at fully and half-filled orbitals. Note that these are the cases where the symmetrization of the solution by averaging over all quantum numbers  $m$  is exact.

A comparison of the exchange energy density with the LSDA and PBE functions for  $N = 132$  is shown in Fig. 10. Based on the coefficients  $A$  and  $\alpha$ , Eqs. (31), (32),

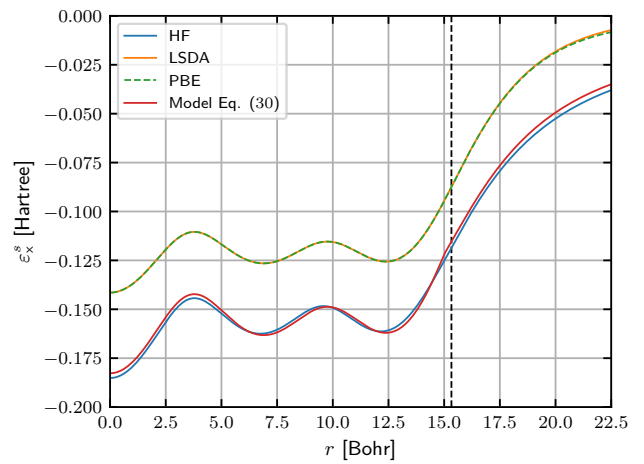


FIG. 10. Spin-dependent one-electron exchange energy density  $\varepsilon_x^s$  calculated by the Hartree-Fock approximation (HF) compared to the models given by LSDA, PBE, and Eq. (30),  $N = 132$ . Vertical dashed line represents the nanoparticle boundary.

we see that LSDA correctly predicts the  $n^{1/3}$  dependence of the energy density inside the nanoparticle, but under-

estimates its magnitude by approximately 24 %. Furthermore, because of the previously mentioned negligible relative gradient of the electron density, PBE does not bring any improvement of the exchange energy density.

From the analysis of the behavior of the fitted parameters, we expect our model to be valid for systems with tens to hundreds of delocalized atomic electrons or, equivalently, nanoparticles of sizes of 1–3 nm. For larger ensembles, the parameter  $A$  is expected to gradually decrease with the LSDA limit of  $3/4 \cdot (3/\pi)^{1/3} \sim 0.739$  for  $N \rightarrow +\infty$ .

## B. Kinetic energy density

Similarly to the exchange energy, we define the one-electron kinetic energy density from the total kinetic energy:

$$E_{\text{kin}} = 4\pi \int_0^{+\infty} \varepsilon_{\text{kin}}(r)n(r)r^2 dr. \quad (36)$$

By matching this to the expression for the kinetic energy given in the Hartree-Fock formalism, we arrive at a defining relation for  $\varepsilon_{\text{kin}}$  in terms of the radial wave functions  $u_{nl}^s$  (see Supplementary Material, Section S3):

$$\varepsilon_{\text{kin}}(r) = -\frac{1}{2} \left[ \sum_{(n,l,s)} N_{nl}^s \left( u_{nl}^s(r) \frac{\partial^2 u_{nl}^s(r)}{\partial r^2} - \frac{l(l+1)}{r^2} u_{nl}^s(r)^2 \right) \right] / \sum_{(n,l,s)} N_{nl}^s u_{nl}^s(r)^2. \quad (37)$$

Fig. 11 shows the kinetic density plotted against the electron density for  $N = 132$ . We see that this time, the energy density inside the nanoparticle is more complex and cannot be simply approximated by one line. We therefore divide the area into two sections:  $(0, r_{\text{lm}}]$  and  $(r_{\text{lm}}, R]$ , where  $r_{\text{lm}}$  denotes the place where the electron density has its last local maximum. For the first part, we fit the kinetic energy density using a power-law function of the form:

$$h(x; D, \varphi) = Dx^\varphi. \quad (38)$$

The second part is fitted together with the outer region with an exponential-type function of the form:

$$j(x; F, G) = \exp(-Fx^{-\omega} - G) \quad (39)$$

Fig. S2 shows the fitted parameters for  $N = 70 - 132$ .

To combine the different behavior in the two distinct areas, we need to gradually transition from the function  $h$  to the function  $j$ . The general formula for the one-electron kinetic energy density depending on the electron density is thus defined as:

$$\varepsilon_{\text{kin}}(r) = (1 - w(r)) h(n(r); D, \varphi) + w(r) j(n(r); F, G, \omega), \quad (40)$$

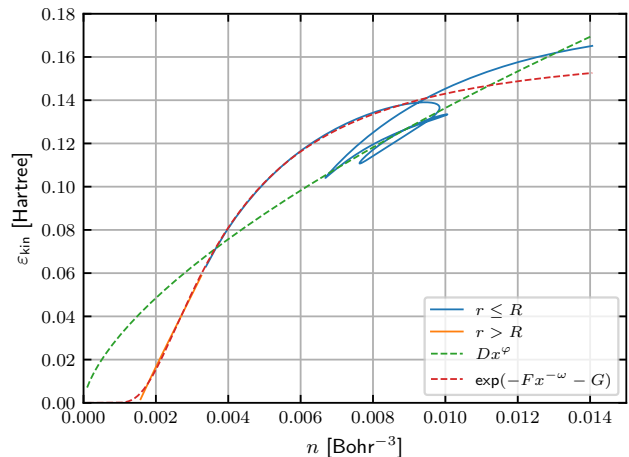


FIG. 11. Dependence of the one-electron kinetic energy density  $\varepsilon_{\text{kin}}(r)$  on the electron density  $n(r)$ . The blue color indicates the inner region of the nanoparticle ( $r \leq R$ ), and orange the outer region ( $r > R$ ). Green and red dashed curves represent the fitted functions  $h$  and  $j$ , with parameters  $D = 2.63$ ,  $\varphi = 0.642$ ,  $F = 4.84 \times 10^{-5}$ ,  $G = 1.800$ , and  $\omega = 1.738$ .

where  $w(r)$  is the first-order smoothstep function centered around the last peak of the electron density given by Eq. (18) interpolating functions  $h$  and  $j$  in the symmetric interval  $[(3\bar{r}_{\text{lm}} - 1)R/2, (\bar{r}_{\text{lm}} + 1)R/2]$ . The parameters  $D$ ,  $\varphi$  and  $F$ ,  $G$ ,  $\omega$  are averaged over the range  $N = 70 - 132$ . The specific values of the means and their standard deviations are as follows:

$$D = 2.91 \pm 0.30, \quad (41)$$

$$\varphi = 0.664 \pm 0.024, \quad (42)$$

$$F = (5.13 \pm 0.55) \times 10^{-5}, \quad (43)$$

$$G = 1.765 \pm 0.018, \quad (44)$$

$$\omega = 1.736 \pm 0.019. \quad (45)$$

As shown in Fig. 12, the absolute percentage error of our model relative to the Hartree-Fock calculations is below 3.2 %, with a mean value of 2.3 %. Interestingly, the local maxima of the error are placed at the fully filled orbitals, whereas the local minima can be found at the half-filled orbitals. This time, the model overestimates the kinetic energy for all cases.

The comparison of the kinetic energy density with the Thomas-Fermi approximation (TF) is shown in Fig. 13. We see that the TF model works well in the area  $(0, r_{\text{lm}}]$ , but quickly loses accuracy near the boundary and outside the nanoparticle.

## VI. CONCLUSION

We have presented a detailed Hartree-Fock analysis of the ground-state electronic structure of spherical gold nanoparticles within the jellium approximation. The

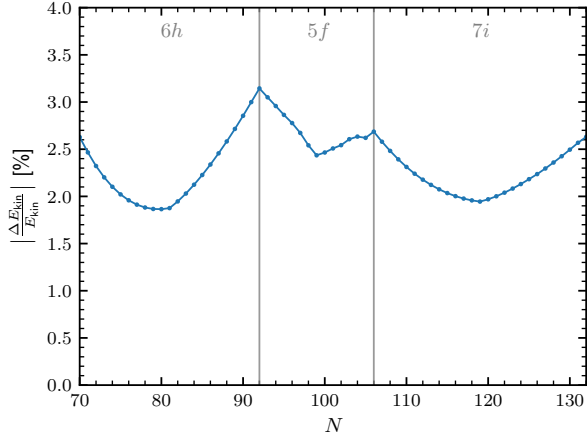


FIG. 12. Absolute percentage error of the total kinetic energy of the model given by Eq. (40) compared to the results of the Hartree-Fock computation. Grey vertical lines represent the cases with fully filled orbitals.

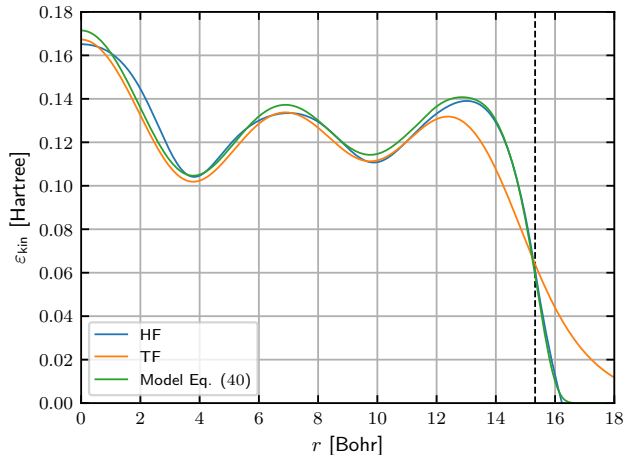


FIG. 13. One-electron kinetic energy density  $\varepsilon_{\text{kin}}$  calculated by the Hartree-Fock approximation (HF) compared to the Thomas-Fermi model (TF) and Eq. (40),  $N = 132$ . Vertical dashed line represents the nanoparticle boundary.

primary objectives of this study were to determine the correct energy-level ordering, accurately characterize the electron density tail and associated negative charge spill-out, and assess the reliability of local models for exchange and kinetic energy potentials. To ensure very high precision, calculations were performed on a real-space grid with a fine step of 0.05 Bohr.

Our results show that the sequence of energy levels follows a pattern that minimizes the quantity  $n - l$  for each principal quantum number  $n$  and maximizes the total spin. This leads to a rather lower number of oscillations of the electron density within the nanoparticle. The specific ordering of the  $(n, l)$ -shells, however, is more complicated and can exhibit slight variations depending on

the chosen Wigner-Seitz radius  $r_s$ .

The asymptotic behavior of the normalized electron density is well captured by an exponential function, with a decay constant linearly dependent on the nanoparticle radius. Consequently, the electronic spill-out exhibits an exponentially decaying dependence on  $R$ , modulated by a rational function.

Based on the calculated electronic structure, we propose improved analytic expressions for the one-electron exchange and kinetic energy densities as explicit functions of the electron density. While the exchange energy maintains the expected  $n^{1/3}$  dependence within the nanoparticle, a significant deviation in the prefactor is observed. This is a direct consequence of the finite size of the system. Moreover, near the surface and beyond, the exchange behavior necessitates an additional exponential-type model. Regarding the kinetic energy, the Thomas-Fermi model yields reasonable results in the interior but fails in the vicinity of the nanoparticle boundary, where an exponential-type model is again required for an accurate description.

This work establishes the foundation for accurate modeling of spherically symmetric confined electronic systems. The proposed exchange and kinetic energy functionals offer potential improvements for classical or orbital-free DFT, quantum hydrodynamics, and semi-classical models. Future investigations will address the incorporation of electron correlation effects and the extension of the model to include structural details.

## VII. METHODS

### A. Discretization of the Wave Functions and the Hamiltonian Operator

To determine the energy levels of the nanoparticle and the corresponding radial wave functions, we employ the *Matrix Method* [23]. This numerical approach is based on discretizing the radial Schrödinger equation within a finite interval  $(0, r_{\text{max}}]$ , assuming that the wave function vanishes at  $r_{\text{max}}$ . The interval is divided into  $M$  subintervals of uniform length  $\Delta r$ . The radial function is discretized into a vector of length  $M$ , where the entries represent the function values at the grid points  $r_k = k\Delta r$ . For notational convenience, we denote the discrete representation of the function by the same symbol, that is,  $u_{nl}[k] \equiv u_{nl}(r_k)$ .

The radial Hamiltonian is then formulated as a matrix  $\mathbb{H} = \mathbb{T} + \mathbb{V}$ . The eigenenergies of the system are obtained as the eigenvalues of  $\mathbb{H}$ , with the corresponding eigenvectors representing the wave functions. The potential term of the Hamiltonian is given by the diagonal matrix:

$$\mathbb{V} = \text{diag}(V_{\text{eff}}(r_1), V_{\text{eff}}(r_2), \dots, V_{\text{eff}}(r_{\text{max}})), \quad (46)$$

where  $V_{\text{eff}}$  is the effective potential defined as:

$$V_{\text{eff}}(r) = \frac{l(l+1)}{2r^2} + V(r), \quad (47)$$

with  $V$  given in Eq. (3) and  $l$  denoting the azimuthal quantum number. The kinetic energy operator is approximated using the central second difference scheme, resulting in a tridiagonal matrix:

$$\mathbb{T} = \frac{1}{2(\Delta r)^2} \begin{pmatrix} 2 & -1 & \dots & 0 \\ -1 & 2 & \dots & 0 \\ \vdots & \vdots & \ddots & \vdots \\ 0 & 0 & \dots & 2 \end{pmatrix}. \quad (48)$$

This formulation reduces the solution of the radial Schrödinger equation to a standard matrix eigenvalue problem which can be solved efficiently using linear algebra routines.

The key advantage of the matrix method is its seamless implementation of the Hartree-Fock equations. This is achieved by discretizing the electron-electron interaction operators  $\hat{V}_H$  and  $\hat{V}_x$  defined by Eqs. (8) and (9). Since  $\hat{V}_H$  acts on the wave function  $u_{nl}^s$  simply by multiplying it by a function  $V_H$ , it can be represented by a diagonal matrix:

$$\mathbb{V}_H = \text{diag}(V_H(r_1), V_H(r_2), \dots, V_H(r_{\max})). \quad (49)$$

In contrast, the exchange potential couples different wave functions at different positions, requiring a full non-trivial matrix representation. To simplify its notation, we partition it into smaller submatrices. The exchange matrix acting on  $u_{nl}^s$  can then be expressed as:

$$\mathbb{V}_x^{ls} = - \sum_{(n', l')} N_{n'l'}^s \sum_{L=|l-l'|}^{l+l'} \begin{pmatrix} l' & L & l \\ 0 & 0 & 0 \end{pmatrix}^2 \mathbb{V}_{n'l's}^L, \quad (50)$$

where the elements of the submatrices  $\mathbb{V}_{n'l's}^L$  are defined as:

$$\mathbb{V}_{n'l's}^L[k, q] = u_{n'l'}^s[k] \frac{\min(k, q)^L}{\max(k, q)^{L+1}} u_{n'l'}^s[q], \quad (51)$$

for  $k, q \in \{1, 2, \dots, M\}$ . This approach once again reduces the solution of the Schrödinger equation to a diagonalization problem, now involving the Hamiltonian matrix  $\mathbb{H}^{ls} = \mathbb{T} + \mathbb{V} + \mathbb{V}_H + \mathbb{V}_x^{ls}$  for each unique one-electron radial wave function  $u_{nl}^s$  in its vector representation.

## B. Implementation of the Hartree-Fock Self-Consistent Cycle

The solution for each  $N$ -electron system consists of three main steps: choosing the appropriate electron configuration by assigning a unique set of quantum numbers to each electron, defining the initial wave functions, and iteratively solving the Hartree-Fock equations until convergence is reached.

We perform the calculations in ascending order of  $N$ , starting with the directly computable one-electron solution. At each increment in  $N$ , if the current energy shell

is not fully occupied, all feasible spin configurations are tested, and the configuration yielding the lowest total energy is selected. When the uppermost shell becomes fully occupied, a new energy level is chosen from the set of unoccupied states, determined by the combinations  $(n, l)$ , up to  $(n_{\max} + 1, l_{\max} + 1)$ , where  $n_{\max}$  and  $l_{\max}$  denote the highest principal and azimuthal quantum numbers used so far.

The initial wave functions are selected at each increment of  $N$  as follows: If no new energy level is introduced (i.e., the added electron remains in the same shell), the solution of the  $(N - 1)$ -electron system is employed as the starting guess. If a higher energy level is required, the initial wave function is chosen as the one-electron solution of the nanoparticle potential with the current radius  $R$ , but the total positive charge reduced to  $Q = 1$ .

After each iteration  $t$ , the wave functions are updated using a weighted sum:

$$u_{nl}^{s,t} = \lambda_t \tilde{u}_{nl}^{s,t} + (1 - \lambda_t) u_{nl}^{s,t-1}, \quad (52)$$

where  $\tilde{u}_{nl}^{s,t}$  is the solution of the Hartree-Fock equations and  $\lambda_t$  is the learning rate defined as:

$$\lambda_t = \max(e^{\alpha(t-1)}, 0.25), \quad (53)$$

with the decay rate  $\alpha = 0.2 \ln 2$ . This adaptive scheme reduces oscillations and stabilizes the computational process. Although the newly computed wave functions  $\tilde{u}_{nl}^{s,t}$  are, in principle, orthogonal, numerical artifacts lead to small deviations from exact orthogonality. To mitigate this issue and restore an orthonormal basis, we apply the Löwdin symmetric orthogonalization procedure [24] to the updated functions  $u_{nl}^{s,t}$ .

For symmetric spin configurations, symmetrization is applied to the converged wave functions and another process of Hartree-Fock calculations is carried out until convergence is achieved. This procedure helps to remove any residual asymmetry producing more physically consistent solutions.

Calculations were carried out for systems with the number of electrons  $N \in \{1, 2, \dots, 132\}$ . To capture the full radial extent of the wave functions, we set  $r_{\max} = 50$  Bohr, significantly exceeding the largest nanoparticle radius in our study,  $R \approx 15.33$  Bohr. The interval  $(0, r_{\max}]$  was discretized into subintervals of length  $\Delta r = 0.05$  Bohr, resulting in the dimension of the wave function vector  $M = 1000$ . This choice of parameters provided sufficient accuracy while maintaining computational feasibility.

Convergence was monitored using three distinct criteria: differences in one-electron energies, wave functions, and electron densities. The conditions for convergence are:

$$|\epsilon_{nl}^t - \epsilon_{nl}^{t-1}| < \varepsilon, \quad (54)$$

$$1 - |\langle u_{nl}^{s,t} | u_{nl}^{s,t-1} \rangle| < \delta, \quad (55)$$

$$\left| \int_0^{+\infty} (u_{nl}^{s,t}(r)^2 - u_{nl}^{s,t-1}(r)^2) \frac{1}{r^2} dr \right| < \gamma, \quad (56)$$

for every electron shell  $(n, l)$ , spin  $s$ , and iteration  $t$ , where the parameters  $\varepsilon = 5 \times 10^{-4}$ ,  $\delta = 1 \times 10^{-4}$ , and  $\gamma = 5 \times 10^{-4}$  were chosen to balance precision with computational efficiency. To avoid excessively long computations, we imposed a maximum of 25 iterations. This upper limit was reached only for certain combinations of quantum numbers  $(n, l)$  that produced non-physical solutions characterized by positive eigenenergies. In all other cases, the procedure converged in 7 to 10 steps.

## ACKNOWLEDGMENT

This work was financially supported by the FerrMion project of the Czech Ministry of Education, co-funded by the EU, Project No. CZ.02.01.01/00/22\_008/0004591; by the Czech Science Foundation (GAČR), Project No. 21-05259S; and by the Student Grant Competition of the Czech Technical University in Prague (SGS), Project No. SGS24/146/OHK4/3T/14.

- 
- [1] L. K. Kelly, E. Coronado, L. L. Zhao, and G. C. Schatz, The optical properties of metal nanoparticles: the influence of size, shape, and dielectric environment, *J. Phys. Chem. B* **107**, 668 (2003).
- [2] I. O. Sosa, C. Noguez, and R. G. Barrera, Optical properties of metal nanoparticles with arbitrary shapes, *J. Phys. Chem. B* **107**, 6269 (2003).
- [3] A. Hernando, P. Crespo, and M. García, Metallic magnetic nanoparticles, *Sci. World J.* **5**, 972 (2005).
- [4] T. Kawawaki and Y. Negishi, Gold nanoclusters as electrocatalysts for energy conversion, *Nanomaterials* **10**, 238 (2020).
- [5] O. Afzal, A. S. Altamimi, M. S. Nadeem, S. I. Alzarea, W. H. Almalki, A. Tariq, B. Mubeen, B. N. Murtaza, S. Iftikhar, N. Riaz, *et al.*, Nanoparticles in drug delivery: From history to therapeutic applications, *Nanomaterials* **12**, 4494 (2022).
- [6] V. Harish, D. Tewari, M. Gaur, A. B. Yadav, S. Swaroop, M. Bechelany, and A. Barhoum, Review on nanoparticles and nanostructured materials: Bioimaging, biosensing, drug delivery, tissue engineering, antimicrobial, and agro-food applications, *Nanomaterials* **12**, 457 (2022).
- [7] M. Bowker, C. O'Rourke, and A. Mills, The role of metal nanoparticles in promoting photocatalysis by tio<sub>2</sub>, *Top. Curr. Chem.* **380**, 17 (2022).
- [8] K. Khurana and N. Jaggi, Localized surface plasmonic properties of au and ag nanoparticles for sensors: a review, *Plasmonics* **16**, 981 (2021).
- [9] N. D. Lang and W. Kohn, Theory of metal surfaces: Charge density and surface energy, *Phys. Rev. B* **1**, 4555 (1970).
- [10] M. Brack, The physics of simple metal clusters: self-consistent jellium model and semiclassical approaches, *Rev. Mod. Phys.* **65**, 677 (1993).
- [11] W. Ekardt, Work function of small metal particles: Self-consistent spherical jellium-background model, *Phys. Rev. B* **29**, 1558 (1984).
- [12] W. Ekardt, Dynamical polarizability of small metal particles: Self-consistent spherical jellium background model, *Phys. Rev. Lett.* **52**, 1925 (1984).
- [13] F. R. Redfern, R. C. Chaney, and P. G. Rudolf, Self-consistent electronic structure of lithium clusters, *Phys. Rev. B* **32**, 5023 (1985).
- [14] W. Knight, W. A. De Heer, W. A. Saunders, K. Clemenger, M. Chou, and M. L. Cohen, Alkali metal clusters and the jellium model, *Chem. Phys. Lett.* **134**, 1 (1987).
- [15] C. Guet and W. R. Johnson, Dipole excitations of closed-shell alkali-metal clusters, *Phys. Rev. B* **45**, 11283 (1992).
- [16] M. S. Hansen and H. Nishioka, Exchange effects on electronic states in jellium clusters, *Z. Phys. D* **28**, 73 (1993).
- [17] M. Madjet, C. Guet, and W. Johnson, Comparative study of exchange-correlation effects on the electronic and optical properties of alkali-metal clusters, *Phys. Rev. A* **51**, 1327 (1995).
- [18] C. Ciraci and F. Della Sala, Quantum hydrodynamic theory for plasmonics: Impact of the electron density tail, *Phys. Rev. B* **93**, 205405 (2016).
- [19] Q. Zhou, W. Li, Z. He, P. Zhang, and X.-W. Chen, Quantum hydrodynamic model for noble metal nanoplasmonics, *Phys. Rev. B* **107**, 205413 (2023).
- [20] R. Esteban, A. G. Borisov, P. Nordlander, and J. Aizpurua, Bridging quantum and classical plasmonics with a quantum-corrected model, *Nat. Commun.* **3**, 825 (2012).
- [21] M. Zapata, Á. S. Camacho Beltrán, A. G. Borisov, and J. Aizpurua, Quantum effects in the optical response of extended plasmonic gaps: validation of the quantum corrected model in core-shell nanomatryushkas, *Opt. Express* **23**, 8134 (2015).
- [22] E. Krotscheck and W. Kohn, Nonlocal screening in metal surfaces, *Phys. Rev. Lett.* **57**, 862 (1986).
- [23] T. Gomez, T. Nagayama, C. Fontes, D. Kilcrease, S. Hansen, M. Montgomery, and D. Winget, Matrix methods for solving hartree-fock equations in atomic structure calculations and line broadening, *Atoms* **6**, 22 (2018).
- [24] P.-O. Löwdin, On the non-orthogonality problem connected with the use of atomic wave functions in the theory of molecules and crystals, *J. Chem. Phys.* **18**, 365 (1950).

## Supplementary Material: Beyond LSDA and Thomas-Fermi: A Hartree-Fock Analysis of Spherical Nanoparticles in the Jellium Approximation

Michael Píro and Jaroslav Hamrle

*Department of Solid State Engineering, Faculty of Nuclear Sciences and  
Physical Engineering, Czech Technical University, Trojanova 13, Prague,  
Czech Republic*

(Dated: 8 July 2025)

### S1. NANOPARTICLE POTENTIAL DERIVATION

For a given charge density distribution  $n_{\text{I}}(\mathbf{r})$ , the electrostatic potential  $V(\mathbf{r})$  is defined as:

$$V(\mathbf{r}) = - \int_{\mathbb{R}^3} \frac{n_{\text{I}}(\mathbf{r}')}{|\mathbf{r}' - \mathbf{r}|} d\mathbf{r}'. \quad (\text{S1})$$

We consider a spherical nanoparticle of radius  $R$ , centered at the origin, with a uniform positive charge density:

$$n_{\text{I}}(\mathbf{r}') = \begin{cases} n_{\text{I}} & |\mathbf{r}'| \leq R \\ 0 & |\mathbf{r}'| > R. \end{cases} \quad (\text{S2})$$

Due to spherical symmetry, the potential depends only on the radial distance  $r = |\mathbf{r}|$ . Without loss of generality, we orient the coordinate system so that  $\mathbf{r}$  lies along the  $z$ -axis. Then for the distance between the vectors  $\mathbf{r}'$ ,  $\mathbf{r}$  we have:

$$|\mathbf{r}' - \mathbf{r}| = \sqrt{r'^2 + r^2 - 2r'r \cos \theta'}, \quad (\text{S3})$$

where  $r' = |\mathbf{r}'|$ . The potential can then become:

$$\begin{aligned} V(r) &= - \int_0^{2\pi} d\phi' \int_0^\pi \int_0^R \frac{n_{\text{I}} r'^2}{\sqrt{r'^2 + r^2 - 2r'r \cos \theta'}} dr' \sin \theta' d\theta' = \\ &= - \frac{2\pi n_{\text{I}}}{r} \int_0^R r' \int_{(r'-r)^2}^{(r'+r)^2} \frac{1}{2\sqrt{t}} dt dr' = - \frac{2\pi n_{\text{I}}}{r} \int_0^R r'(r' + r - |r' - r|) dr', \end{aligned} \quad (\text{S4})$$

where the substitution  $t = r'^2 + r^2 - 2r'r \cos \theta$  was used in the second step. We now distinguish two cases:

1.  $r \leq R$ :

$$V(r) = - \frac{2\pi n_{\text{I}}}{r} \left( \int_0^r 2r'^2 dr' + \int_r^R 2r' r dr' \right) = - \frac{2\pi n_{\text{I}}}{3} (3R^2 - r^2), \quad (\text{S5})$$

2.  $r > R$ :

$$V(r) = - \frac{2\pi n_{\text{I}}}{r} \int_0^R 2r'^2 dr' = - \frac{4}{3} \pi R^3 \frac{n_{\text{I}}}{r}. \quad (\text{S6})$$

Now we just use the fact, that the total charge of the particle  $Q = \frac{4}{3} \pi R^3 n_{\text{I}}$  and we arrive at:

$$V(r) = \begin{cases} \frac{Q}{2R^3} r^2 - \frac{3Q}{2R} & r \leq R \\ -\frac{Q}{r} & r > R. \end{cases} \quad (\text{S7})$$

Let us add two more notes on the general form of the potential. We see that it is parameterized by the total charge  $Q$  and the radius of the nanoparticle  $R$ . The charge is given by:

$$Q = N\nu, \quad (\text{S8})$$

where  $N$  is the number of atoms and  $\nu$  is the number of electrons per atom, which are considered not bound to the nucleus. Secondly, since we assume, that the atoms of the particle are arranged in a crystal lattice, constants  $N$  and  $R$  are not independent, but related by the expression:

$$R = r_s N^{1/3}, \quad (\text{S9})$$

where  $r_s$  is the so-called Wigner-Seitz radius. This means that for a given material, the potential can be described by only one parameter, usually the radius  $R$ . Putting it all together, we obtain the final form of the potential:

$$V(r) = \begin{cases} \frac{\nu}{r_s^3} \frac{r^2 - 3R^2}{2} & r \leq R \\ -\frac{\nu}{r_s^3} \frac{R^3}{r} & r > R. \end{cases} \quad (\text{S10})$$

The electrostatic energy of this charged ball can be calculated as:

$$E_I = -\frac{1}{2} \int_{\mathbb{R}^3} V(\mathbf{r}) n_I(\mathbf{r}) d\mathbf{r} = -2\pi n_I \int_0^R V(r) r^2 dr. \quad (\text{S11})$$

Using Eq. S10 and the fact that the uniform ionic density can be expressed in terms of  $\nu$  and  $r_s$  as:

$$n_I = \frac{3\nu}{4\pi r_s^3}, \quad (\text{S12})$$

we arrive at the expression for the ionic energy:

$$E_I = \frac{3\nu^2 R^5}{5r_s^6}, \quad (\text{S13})$$

or equivalently in terms of the number of electrons  $N$ :

$$E_I = \frac{3\nu^2}{5r_s} N^{\frac{5}{3}}. \quad (\text{S14})$$

## S2. RADIAL ELECTRON-ELECTRON INTERACTION POTENTIALS

The total electron–electron interaction energy for a system of  $N$  electrons  $\{\psi_i\}_{i=1}^N$  is given by:

$$E_{e-e} = \frac{1}{2} \sum_{i=1}^N \langle \psi_i | \hat{V}_H + \hat{V}_x | \psi_i \rangle, \quad (\text{S15})$$

where the Hartree and exchange potentials are defined as:

$$\hat{V}_H \psi_i(\mathbf{r}) = \sum_{j=1}^N \int_{\mathbb{R}^3} \psi_j^*(\mathbf{r}') V_2(\mathbf{r}, \mathbf{r}') \psi_j(\mathbf{r}') d\mathbf{r}' \psi_i(\mathbf{r}), \quad (\text{S16})$$

$$\hat{V}_x \psi_i(\mathbf{r}) = -\sum_{j=1}^N \delta_{s_i s_j} \int_{\mathbb{R}^3} \psi_j^*(\mathbf{r}') V_2(\mathbf{r}, \mathbf{r}') \psi_i(\mathbf{r}') d\mathbf{r}' \psi_j(\mathbf{r}), \quad (\text{S17})$$

with  $s_i$  denoting the spin of the wave function  $\psi_i$  and the two-electron potential  $V_2$  defined as:

$$V_2(\mathbf{r}, \mathbf{r}') = \frac{1}{|\mathbf{r} - \mathbf{r}'|}. \quad (\text{S18})$$

To exploit the spherical symmetry, we expand  $V_2$  using the *generating function of Legendre polynomials*:

$$V_2(\mathbf{r}, \mathbf{r}') = \frac{1}{\sqrt{r^2 + r'^2 - 2rr' \cos \vartheta}} = \sum_{l=0}^{+\infty} P_l(\cos \vartheta) \frac{\min(r, r')^l}{\max(r, r')^{l+1}}, \quad (\text{S19})$$

where  $r = |\mathbf{r}|$ ,  $r' = |\mathbf{r}'|$ , and  $\vartheta$  is the angle between  $\mathbf{r}$  and  $\mathbf{r}'$ . Next, we rewrite the polynomials  $P_l$  with the help of the *addition theorem of spherical harmonics*:

$$P_l(\cos \vartheta) = \frac{4\pi}{2l+1} \sum_{m=-l}^l Y_l^{m*}(\theta, \phi) Y_l^m(\theta', \phi'), \quad (\text{S20})$$

where  $\theta$ ,  $\phi$ , and  $\theta'$ ,  $\phi'$  are the angles of  $\mathbf{r}$  and  $\mathbf{r}'$  in their common spherical coordinates. From there,  $V_2$  can be expressed as:

$$V_2(\mathbf{r}, \mathbf{r}') = \sum_{l=0}^{+\infty} \sum_{m=-l}^l \frac{4\pi}{2l+1} Y_l^{m*}(\theta, \phi) Y_l^m(\theta', \phi') \frac{\min(r, r')^l}{\max(r, r')^{l+1}}. \quad (\text{S21})$$

The one-electron wave functions are written in the separable form:

$$\psi_{nlm}^s(r, \theta, \phi) = \frac{1}{r} u_{nl}^s(r) Y_l^m(\theta, \phi). \quad (\text{S22})$$

Inserting Eqs. (S21), (S22), and converting the electron index summation to a sum over quantum numbers  $(n', l', m', s')$ , the Hartree potential becomes:

$$\begin{aligned} \hat{V}_H \psi_{nlm}^s(r, \theta, \phi) &= \sum_{(n', l', m', s')} \sum_{L=0}^{+\infty} \sum_{M=-L}^L \frac{4\pi}{2L+1} \int_0^{+\infty} u_{n'l'}^{s'}(r')^2 \frac{\min(r, r')^L}{\max(r, r')^{L+1}} dr' \\ &\cdot \int_{\Omega} Y_{l'}^{m'*}(\theta', \phi') Y_L^M(\theta', \phi') Y_{l'}^{m'}(\theta', \phi') \sin \theta' d\theta' d\phi' Y_L^{M*}(\theta, \phi) \psi_{nlm}^s(r, \theta, \phi). \end{aligned} \quad (\text{S23})$$

The angular integral can be evaluated using the standard identity:

$$\begin{aligned} \int_{\Omega} Y_{l_1}^{m_1*}(\theta, \phi) Y_{l_2}^{m_2}(\theta, \phi) Y_{l_3}^{m_3}(\theta, \phi) \sin \theta d\theta d\phi &= \\ &= (-1)^{m_1} \sqrt{\frac{(2l_1+1)(2l_2+1)(2l_3+1)}{4\pi}} \begin{pmatrix} l_1 & l_2 & l_3 \\ 0 & 0 & 0 \end{pmatrix} \begin{pmatrix} l_1 & l_2 & l_3 \\ -m_1 & m_2 & m_3 \end{pmatrix}, \end{aligned} \quad (\text{S24})$$

where  $\begin{pmatrix} a & b & c \\ d & e & f \end{pmatrix}$  denotes the *Wigner 3-j symbol*. We can write:

$$\begin{aligned} \hat{V}_H \psi_{nlm}^s(r, \theta, \phi) &= \sum_{(n', l', m', s')} \sum_{L=0}^{+\infty} \sum_{M=-L}^L (-1)^{m'} (2l'+1) \sqrt{\frac{4\pi}{2L+1}} \begin{pmatrix} l' & L & l' \\ 0 & 0 & 0 \end{pmatrix} \\ &\cdot \begin{pmatrix} l' & L & l' \\ -m' & M & m' \end{pmatrix} \int_0^{+\infty} u_{n'l'}^{s'}(r')^2 \frac{\min(r, r')^L}{\max(r, r')^{L+1}} dr' Y_L^{M*}(\theta, \phi) \psi_{nlm}^s(r, \theta, \phi). \end{aligned} \quad (\text{S25})$$

Similarly, for the exchange potential, we have:

$$\begin{aligned} \hat{V}_x \psi_{nlm}^s(r, \theta, \phi) = & - \sum_{(n', l', m')} \sum_{L=0}^{+\infty} \sum_{M=-L}^L (-1)^{m'} \sqrt{(2l'+1)(2l+1)} \sqrt{\frac{4\pi}{2L+1}} \cdot \\ & \cdot \begin{pmatrix} l' & L & l \\ 0 & 0 & 0 \end{pmatrix} \begin{pmatrix} l' & L & l \\ -m' & M & m \end{pmatrix} \cdot \\ & \cdot \int_0^{+\infty} u_{nl}^s(r') u_{n'l'}^s(r') \frac{\min(r, r')^L}{\max(r, r')^{L+1}} dr' Y_L^{M*}(\theta, \phi) \psi_{n'l'm'}^s(r, \theta, \phi). \end{aligned} \quad (\text{S26})$$

Since the angular part of the wave function does not change during the Hartree-Fock procedure and we want to express the electron-electron interaction potentials only as operators acting on the radial part of the wave function, we rewrite the expression for the interaction energy given by Eq. (S15) as:

$$E_{e-e} = \frac{1}{2} \sum_{(n, l, m, s)} \langle \psi_{nlm}^s | \hat{V}_H + \hat{V}_x | \psi_{nlm}^s \rangle = \frac{1}{2} \sum_{(n, l, s)} \langle u_{nl}^s | \sum_m \langle Y_l^m | \hat{V}_H + \hat{V}_x | Y_l^m \rangle | u_{nl}^s \rangle. \quad (\text{S27})$$

Note that the  $1/r$  prefactors in the wave functions cancel the Jacobian  $r^2$ , so we do not explicitly write them out and handle the final integration over  $r$  as a simple 1D integration with no additional factors. Together with Eq. S24 we arrive at the expression:

$$\begin{aligned} \sum_m \langle Y_l^m | \hat{V}_H | Y_l^m \rangle | u_{nl}^s \rangle = & \sum_m \sum_{(n', l', m', s')} \sum_{L=0}^{+\infty} \sum_{M=-L}^L (-1)^{m+m'} (2l+1)(2l'+1) \cdot \\ & \cdot \begin{pmatrix} l & L & l \\ 0 & 0 & 0 \end{pmatrix} \begin{pmatrix} l & L & l \\ -m & M & m \end{pmatrix} \begin{pmatrix} l' & L & l' \\ 0 & 0 & 0 \end{pmatrix} \begin{pmatrix} l' & L & l' \\ -m' & M & m' \end{pmatrix} \cdot \\ & \cdot \int_0^{+\infty} u_{n'l'}^s(r')^2 \frac{\min(r, r')^L}{\max(r, r')^{L+1}} dr' u_{nl}^s(r). \end{aligned} \quad (\text{S28})$$

Similarly, for the exchange potential we get:

$$\begin{aligned} \sum_m \langle Y_l^m | \hat{V}_x | Y_l^m \rangle | u_{nl}^s \rangle = & - \sum_m \sum_{(n', l', m')} \sum_{L=0}^{+\infty} \sum_{M=-L}^L (2l+1)(2l'+1) \cdot \\ & \cdot \begin{pmatrix} l' & L & l \\ 0 & 0 & 0 \end{pmatrix}^2 \begin{pmatrix} l' & L & l \\ -m' & M & m \end{pmatrix}^2 \cdot \\ & \cdot \int_0^{+\infty} u_{nl}^s(r') u_{n'l'}^s(r') \frac{\min(r, r')^L}{\max(r, r')^{L+1}} dr' u_{n'l'}^s(r). \end{aligned} \quad (\text{S29})$$

Several simplifications can be made now. First, the second row of the Wigner 3-j symbol must sum up to zero. Therefore, the only valid values for the number  $M$  are zero for the Hartree potential and  $m' - m$  for the exchange potential. Secondly, at this stage, we consider every electron shell  $(n, l)$  to be fully filled, i.e. the summations over the magnetic quantum numbers  $m$  and  $m'$  use all values between  $-l$  and  $l$ , and  $-l'$  and  $l'$ , respectively. This allows us to use the following summation formulas for the Wigner 3-j symbols:

$$\sum_{m=-l}^l (-1)^m \begin{pmatrix} l & L & l \\ -m & 0 & m \end{pmatrix} = (-1)^l \sqrt{2l+1} \delta_{L0}, \quad (\text{S30})$$

$$\sum_{m=-l}^l \sum_{m'=-l'}^{l'} \begin{pmatrix} l' & L & l \\ -m' & m' - m & m \end{pmatrix}^2 = 1 \quad (\text{S31})$$

followed by the simple relation:

$$\begin{pmatrix} l & 0 & l \\ 0 & 0 & 0 \end{pmatrix} = (-1)^l \frac{1}{\sqrt{2l+1}}. \quad (\text{S32})$$

Finally, the numbers in the first row of the Wigner 3-j symbol must obey the triangular inequality, yielding limits on the summation over  $L$ . The resulting relations for the two potentials acting on a single electron from the shell  $(n, l)$  are of the form:

$$\hat{V}_H^{(\text{rad})} u_{nl}^s(r) = \sum_{(n', l', s')} (2l' + 1) \int_0^{+\infty} u_{n'l'}^{s'}(r')^2 \frac{1}{\max(r, r')} dr' u_{nl}^s(r), \quad (\text{S33})$$

and

$$\begin{aligned} \hat{V}_x^{(\text{rad})} u_{nl}^s(r) = & - \sum_{(n', l')} (2l' + 1) \sum_{L=|l-l'|}^{l+l'} \begin{pmatrix} l' & L & l \\ 0 & 0 & 0 \end{pmatrix}^2 \\ & \cdot \int_0^{+\infty} u_{nl}^s(r') u_{n'l'}^s(r') \frac{\min(r, r')^L}{\max(r, r')^{L+1}} dr' u_{n'l'}^s(r), \end{aligned} \quad (\text{S34})$$

where the radial one electron potentials are defined as:

$$\hat{V}_H^{(\text{rad})} = \frac{1}{2l+1} \sum_m \langle Y_l^m | \hat{V}_H | Y_l^m \rangle, \quad (\text{S35})$$

$$\hat{V}_x^{(\text{rad})} = \frac{1}{2l+1} \sum_m \langle Y_l^m | \hat{V}_x | Y_l^m \rangle. \quad (\text{S36})$$

In the main text, however, we use the same symbols for the radial potentials as for the full interaction potentials for notational simplicity.

Lastly, if the shells are not fully filled, we consider the electrons equally distributed over all possible quantum numbers  $m$ . The result therefore stays the same with only the multiplicity changing from  $(2l+1)$  to  $N_{nl}^s$  denoting the actual number of electrons in the shell  $(n, l)$  with spin  $s$ .

### S3. EXCHANGE AND KINETIC ENERGY DENSITIES AS FUNCTIONS OF THE ELECTRON DENSITY

To find a formula for the exchange energy density as a function of the electron density, we start by defining the spin-dependent one-electron exchange energy field  $\varepsilon_x^s$  from the total exchange energy:

$$E_x = \sum_s \int_{\mathbb{R}^3} \varepsilon_x^s(\mathbf{r}) n^s(\mathbf{r}) d\mathbf{r}, \quad (\text{S37})$$

where the total electron density of the electrons with spin  $s$  is defined in terms of the one-electron wave functions as:

$$n^s(\mathbf{r}) = \sum_{(n, l, m)} |\psi_{nlm}^s(\mathbf{r})|^2. \quad (\text{S38})$$

In the case of not fully filled orbitals, we consider the wave functions to be equally distributed over all possible quantum numbers  $m$ . Therefore, we can assume spherical symmetry for all cases, and hence the electron density depends only on the radial coordinate  $r$ :

$$n^s(r) \equiv n^s(r, \theta, \phi) = \sum_{(n, l, m)} \frac{1}{r^2} u_{nl}^s(r)^2 |Y_l^m(\theta, \phi)|^2 = \sum_{(n, l)} N_{nl}^s \frac{u_{nl}^s(r)^2}{4\pi r^2}. \quad (\text{S39})$$

Using this, we can rewrite Eq. S37 in spherical coordinates as:

$$E_x = \sum_{(n,l,s)} N_{nl}^s \int_0^{+\infty} \varepsilon_x^s(r) u_{nl}^s(r)^2 dr. \quad (\text{S40})$$

On the other hand, from the Eqs. (S27) and (S34) we can express the total exchange energy from our Hartree-Fock calculations as:

$$\begin{aligned} E_x &= \frac{1}{2} \sum_{(n,l,s)} N_{nl}^s \langle u_{nl}^s | \hat{V}_x^{(\text{rad})} | u_{nl}^s \rangle = \\ &= -\frac{1}{2} \sum_{(n,l,s)} N_{nl}^s \sum_{(n',l')} N_{n'l'}^s \sum_{L=|l-l'|}^{l+l'} \binom{l' \ L \ l}{0 \ 0 \ 0}^2 \cdot \\ &\quad \cdot \int_0^{+\infty} \int_0^{+\infty} u_{nl}^s(r') u_{n'l'}^s(r') \frac{\min(r,r')^L}{\max(r,r')^{L+1}} dr' u_{nl}^s(r) u_{n'l'}^s(r) dr. \end{aligned} \quad (\text{S41})$$

By comparing the relations for the total exchange energy, we arrive at the final expression for the one-electron exchange field:

$$\begin{aligned} \varepsilon_x^s(r) &= -\frac{1}{2} \left[ \sum_{(n,l)} N_{nl}^s \sum_{(n',l')} N_{n'l'}^s \sum_{L=|l-l'|}^{l+l'} \binom{l' \ L \ l}{0 \ 0 \ 0}^2 \cdot \right. \\ &\quad \left. \cdot \int_0^{+\infty} u_{nl}^s(r') u_{n'l'}^s(r') \frac{\min(r,r')^L}{\max(r,r')^{L+1}} dr' u_{nl}^s(r) u_{n'l'}^s(r) \right] / \sum_{(n,l)} N_{nl}^s u_{nl}^s(r)^2. \end{aligned} \quad (\text{S42})$$

The next step is to find a good approximation of the exchange energy density as a function of the electron density, i.e. the function  $\varepsilon_x^s(n^s)$  satisfying:

$$\varepsilon_x^s(n^s(r)) \approx \varepsilon_x^s(r). \quad (\text{S43})$$

The functional of the exchange energy then becomes:

$$E_x[n^\uparrow, n^\downarrow] = 4\pi \sum_s \int_0^{+\infty} \varepsilon_x^s(n^s(r)) n^s(r) r^2 dr, \quad (\text{S44})$$

and we can define the spin-dependent exchange potential function  $V_x^s(n)$  as:

$$V_x^s(n^s) = \frac{\delta E_x[n^\uparrow, n^\downarrow]}{\delta n^s} = \varepsilon_x^s(n^s) + n^s \frac{d\varepsilon_x^s(n^s)}{dn^s}. \quad (\text{S45})$$

Similarly, we can define the one-electron kinetic energy density  $\varepsilon_{\text{kin}}$  via the total kinetic energy  $E_{\text{kin}}$ :

$$E_{\text{kin}} = \int_{\mathbb{R}^3} \varepsilon_{\text{kin}}(\mathbf{r}) n(\mathbf{r}) d\mathbf{r} = \sum_{(n,l,s)} N_{nl}^s \int_0^{+\infty} \varepsilon_{\text{kin}}(r) u_{nl}^s(r)^2 dr. \quad (\text{S46})$$

From the Hartree-Fock approximation, we can rewrite the total kinetic energy as follows:

$$\begin{aligned} E_{\text{kin}} &= \sum_{i=1}^N \langle \psi_i | \hat{T} | \psi_i \rangle = -\frac{1}{2} \sum_{(n,l,s)} N_{nl}^s \left\langle u_{nl}^s \left| \frac{\partial^2}{\partial r^2} - \frac{l(l+1)}{r^2} \right| u_{nl}^s \right\rangle = \\ &= -\frac{1}{2} \sum_{(n,l,s)} N_{nl}^s \int_0^{+\infty} \left( u_{nl}^s(r) \frac{\partial^2 u_{nl}^s(r)}{\partial r^2} - \frac{l(l+1)}{r^2} u_{nl}^s(r)^2 \right) dr. \end{aligned} \quad (\text{S47})$$

Therefore, the kinetic density can be expressed as:

$$\varepsilon_{\text{kin}}(r) = -\frac{1}{2} \left[ \sum_{(n,l,s)} N_{nl}^s \left( u_{nl}^s(r) \frac{\partial^2 u_{nl}^s(r)}{\partial r^2} - \frac{l(l+1)}{r^2} u_{nl}^s(r)^2 \right) \right] / \sum_{(n,l,s)} N_{nl}^s u_{nl}^s(r)^2. \quad (\text{S48})$$

## S4. FIGURES

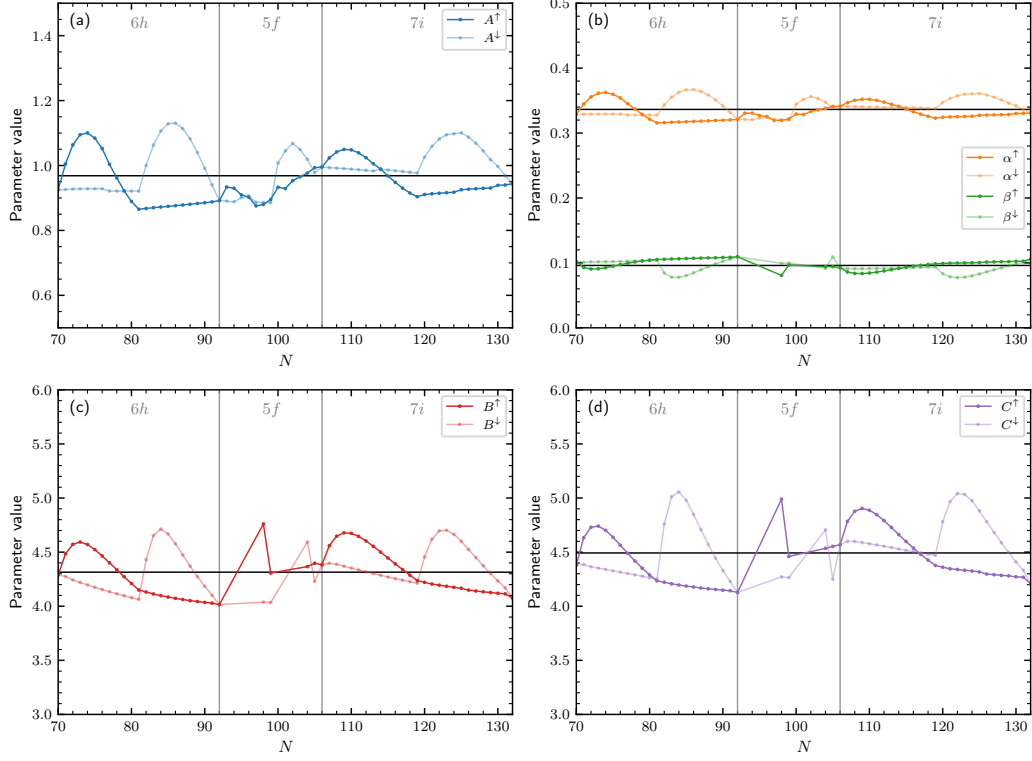


FIG. S1. Dependence of the fitted parameters  $A$  and  $\alpha$  for the function  $f(x) = Ax^\alpha$ , and parameters  $B$ ,  $C$ , and  $\beta$  for the function  $g(x) = \exp(Bx^\beta - C)$ , on the number of electrons  $N$ , describing the exchange energy density model given by Eq. (40). Cases with  $N = 93 - 97$ ,  $100 - 103$  are excluded for parameters  $B$ ,  $C$ , and  $\beta$  due to poor fitting convergence. Dependence of the parameters is shown for both spin orientations. Black horizontal lines show the averages over  $N$  and the spin orientations. The vertical regions denote the different energy shells.

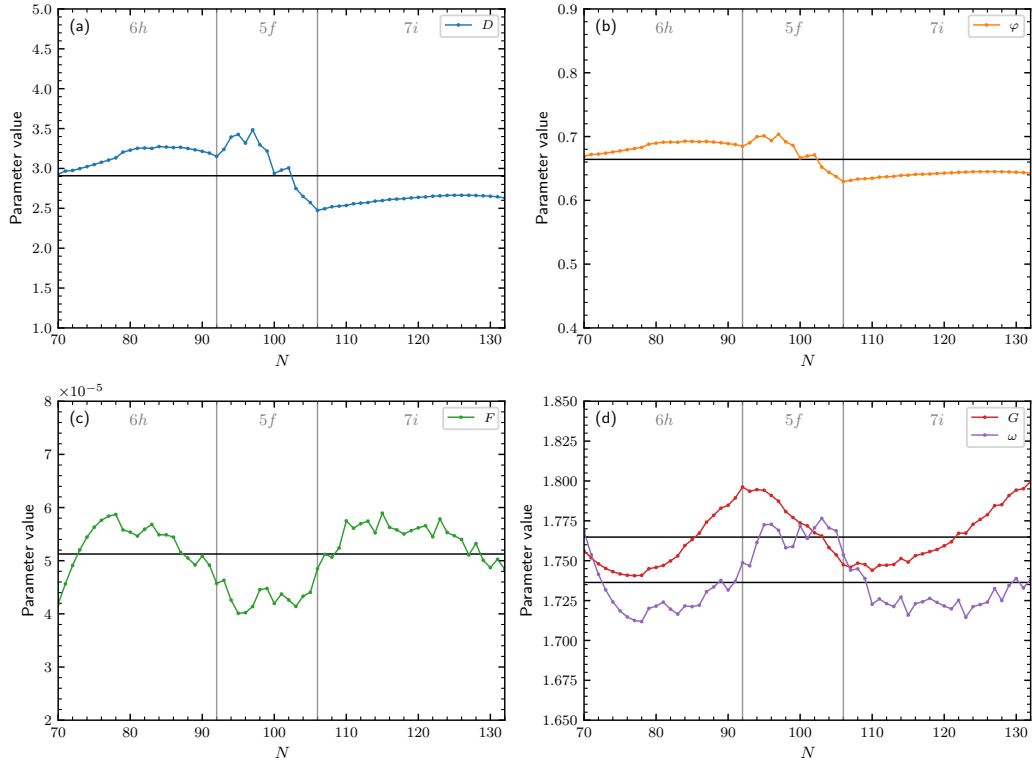


FIG. S2. Dependence of the fitted parameters  $A$  and  $\alpha$  for the function  $f(x) = Ax^\alpha$ , and parameters  $B$ ,  $C$ , and  $\beta$  for the function  $g(x) = \exp(Bx^\beta - C)$ , on the number of electrons  $N$ , describing the kinetic energy density model given by Eq. (40). Cases with  $N = 93 - 97$ ,  $100 - 103$  are excluded for parameters  $B$ ,  $C$ , and  $\beta$  due to poor fitting convergence. Dependence of the parameters is shown for both spin orientations. Black horizontal lines show the averages over  $N$  and the spin orientations. The vertical regions denote the different energy shells.